Bulk ion acceleration and particle heating during magnetic reconnection in a laboratory plasma[a)]

Jongsoo Yoo,[b)] Masaaki Yamada, Hantao Ji, Jonathan Jara-Almonte, and Clayton E. Myers
Center for Magnetic Self-Organization, Princeton Plasma Physics Laboratory, Princeton, New Jersey 08543, USA

(Received 20 January 2014; accepted 20 February 2014; published online 7 May 2014)

Bulk ion acceleration and particle heating during magnetic reconnection are studied in the collisionless plasma of the Magnetic Reconnection Experiment (MRX). The plasma is in the two-fluid regime, where the motion of the ions is decoupled from that of the electrons within the ion diffusion region. The reconnection process studied here is quasi-symmetric since plasma parameters such as the magnitude of the reconnecting magnetic field, the plasma density, and temperature are compatible on each side of the current sheet. Our experimental data show that the in-plane (Hall) electric field plays a key role in ion heating and acceleration. The electrostatic potential that produces the in-plane electric field is established by electrons that are accelerated near the electron diffusion region. The in-plane profile of this electrostatic potential shows a "well" structure along the direction normal to the reconnection current sheet. This well becomes deeper and wider downstream as its boundary expands along the separatrices where the in-plane electric field is strongest. Since the in-plane electric field is 3–4 times larger than the out-of-plane reconnection electric field, it is the primary source of energy for the unmagnetized ions. With regard to ion acceleration, the Hall electric field causes ions near separatrices to be ballistically accelerated toward the outflow direction. Ion heating occurs as the accelerated ions travel into the high pressure downstream region. This downstream ion heating cannot be explained by classical, unmagnetized transport theory; instead, we conclude that ions are heated by re-magnetization of ions in the reconnection exhaust and collisions. Two-dimensional (2-D) simulations with the global geometry similar to MRX demonstrate downstream ion thermalization by the above mechanisms. Electrons are also significantly heated during reconnection. The electron temperature sharply increases across the separatrices and peaks just outside of the electron diffusion region. Unlike ions, electrons acquire energy mostly from the reconnection electric field, and the energy gain is localized near the X-point. However, the increase in the electron bulk flow energy remains negligible. These observations support the assertion that efficient electron heating mechanisms exist around the electron diffusion region and that the heat generated there is quickly transported along the magnetic field due to the high parallel thermal conductivity of electrons. Classical Ohmic dissipation based on the perpendicular Spitzer resistivity is too small to balance the measured heat flux, indicating the presence of anomalous electron heating. © *2014 AIP Publishing LLC*.
[http://dx.doi.org/10.1063/1.4874331]

I. INTRODUCTION

Magnetic reconnection is recognized as a fundamental process in magnetized plasmas, whether in the laboratory, the solar system, or distant objects in the universe.[1–3] Reconnection is responsible for sawtooth relaxations in a tokamak, a toroidal device used in thermonuclear fusion experiments.[4] It is also widely believed that reconnection plays a key role in dynamic phenomena in the solar system, such as solar flares, coronal mass ejections, and magnetospheric substorms, as well as in astrophysical plasmas, such as stellar flares and outbursts generated in accretion disks.[1–3]

One of the most important aspects of magnetic reconnection is its ability to efficiently convert magnetic energy to particle energy. In the Sweet-Parker model based on resistive magnetohydrodynamics (MHD),[5,6] Ohmic dissipation is the major energy conversion mechanism. However, classical Ohmic dissipation is not the dominant energy conversion mechanism during collisionless reconnection where electrons and ions move differently such that two-fluid effects become important. Since most reconnection layers in nature are in the two-fluid regime, identifying key energy conversion processes for both electrons and ions during two-fluid reconnection is essential to understand the explosive phenomena that are associated with magnetic reconnection.

Ion acceleration associated with reconnection has been widely observed in space. In the Earth's magnetosphere, Alfvénic ion jets have been attributed to reconnection outflows [e.g., Refs. 7–10]. The in-plane (Hall) electric field has been identified as the cause of bulk ion acceleration to speeds approaching the Alfvén velocity $V_A \equiv B/\sqrt{\mu_0 m_i n_i}$, where m_i is the ion mass and n_i is the ion number density.[11] The Hall electric field is electrostatic and mostly

[a)]Paper DI3 3, Bull. Am. Phys. Soc. **58**, 101 (2013).
[b)]Invited speaker.

perpendicular to the local magnetic field. It is strongest near the separatrices and negligible upstream. The component of the Hall electric field normal to the current sheet is bipolar; it points toward the current sheet. Thus, the in-plane potential profile shows a well structure along the direction normal to the current sheet. Along with the quadrupole out-of-plane magnetic field, the in-plane electric field is considered to be a signature of two-fluid effects. The aforementioned potential well structure has been observed in the magnetosphere [e.g., Refs. 12 and 13] and in many numerical simulations [e.g., Refs. 14–18].

Direct ion acceleration by the Hall electric field has not previously been observed in laboratory plasmas. The in-plane electric field during reconnection was indirectly measured in early reconnection experiments at UCLA by measuring $\mathbf{J} \times \mathbf{B}$ and ∇p.[19] The measured in-plane ion flow pattern is qualitatively similar to that observed in numerical simulations [e.g., Refs. 14 and 15]. However, no significant ion acceleration was observed and it was claimed that anomalous scattering by waves was responsible for the measured slow ion outflow. Ion flow speeds close to V_A were observed during spheromak merging experiments,[20,21] but ion acceleration mechanisms were not identified. In this paper, the first simultaneous laboratory measurement of both the Hall electric field and ion acceleration toward the outflow direction are presented.

Despite many observations of ion heating in laboratory plasmas during reconnection, the mechanisms behind the observed ion heating remain unresolved. In the TS-3 device at the University of Tokyo, the observed global ion heating was attributed to thermalization of sheared Alfvénic flows generated by the so-called "slingshot" effect.[22] More recently, ion heating downstream of the X-point was explained in terms of a fast shock or viscous damping of the reconnection outflow.[21] However, MHD analysis was not fully valid in the plasma due to the small machine size, and no quantitative analysis was made to verify the suggested mechanisms. Moreover, other possibilities exist, such as compressional heating and/or conversion of the translational energy of the merging spheromaks, since the observed ion heating occurred during fast merging of two spheromaks. In the low β plasmas of the Versatile Toroidal Facility (VTF) device at the Massachusetts Institute of Technology, ions are heated from 0.3 to about 2 eV by interactions with the in-plane electric field.[23] However, the observed ion heating is small compared to the electron temperature (20 eV). Moreover, the measured in-plane electric field profiles are different from those seen in numerical simulations, indicating that effects unique to the VTF device such as boundary conditions may play a role. In previous measurements in Magnetic Reconnection Experiment (MRX), ion heating in the reconnection layer was attributed to unknown non-classical mechanisms.[24] In the Madison Symmetric Torus (MST), a reversed field pinch (RFP) device, ion heating related to a drop in stored magnetic energy is observed,[25] but the heating mechanisms have not been conclusively identified. Mass-dependent ion heating was reported,[26] and stochastic heating was postulated. Recently, anisotropic ion heating and superthermal tail generation during the development of non-linear tearing modes were measured,[27] but still the energization processes remained unknown.

A sharp ion temperature increase across the separatrices of the reconnection region has been observed in many simulations [e.g., Refs. 28 and 29]. It is believed that the direct interaction of ions with the in-plane electric field is responsible for the observed ion temperature increase. First, the strong Hall electric field generates various non-Maxwellian ion distributions in the reconnection layer, which can significantly increase the local ion pressure. Four different types of highly structured ion distribution functions in kinetic simulations have been identified and successfully compared to observations from the Geotail satellite.[28] Another possible mechanism, the so-called "pick-up" model for ion heating has been suggested.[29] In this model, cold, unmagnetized ions that cross the reconnection separatrix are suddenly accelerated by the strong in-plane electric field. As ions are re-magnetized downstream, they attain not only the Alfvénic flow velocity but also an equal thermal velocity, which is similar to the classical pick-up process.[30] Comparison with solar wind data from the ACE and Wind spacecraft shows that the observed temperature increment is proportional to ion mass, which agrees with the pick-up model. The magnitude of the measured temperature increments, on the other hand, are consistently lower than predicted by the model.

So far, many observations have suggested that a significant fraction of the energy released during reconnection is converted to ion thermal energy, especially in laboratory plasmas. Many possible mechanisms have been suggested including the damping of Alfvénic fluctuations, viscous damping of flows, stochastic heating, and the pick-up process. To verify ion thermalization processes during reconnection, more quantitative analysis based on data measured in a reconnection layer is required and this paper provides some of the much-needed analysis.

In addition to ion heating and acceleration, electron heating related to magnetic reconnection was observed in early reconnection experiments with a large guide field at UCLA.[31] It was found that magnetic energy was mostly converted to electron thermal energy and that anomalous resistivity (resistivity larger than the classical Spitzer value) existed in the current sheet. More recently, non-classical electron heating in the collisionless reconnection layer of MRX was reported, based on one-dimensional measurements and assumptions on the upstream electron temperature.[32] Classical Ohmic heating was estimated to account for only about 20% of the heat flux required to sustain the observed electron temperature profile, which peaks at the center of the reconnection layer. Strong electromagnetic fluctuations were observed at the same time, such that the observed heating could result from wave-particle interactions; this assertion was not proven quantitatively. Electron heating at the reconnection layer was also observed in TS-3.[21] It was postulated that electrons were heated Ohmically, but no quantitative analysis was provided. In the Earth's magnetotail, a statistical survey on electron temperature as a function of distance from the X-point was conducted.[33] Interestingly, high electron temperature is observed in downstream regions somewhat away from the X-point.

So far, few mechanisms have been suggested for non-classical electron heating during collisionless reconnection. Possible candidates include anisotropic heating by mirror trapping and the parallel electric field[34] and anomalous resistivity due to high-frequency fluctuations.[31,32]

It is important to identify mechanisms for observed non-classical electron heating in laboratory plasmas since it is related to the physics that actually breaks magnetic field lines at the X-point. The observations of non-classical heating indicate the existence of efficient thermalization mechanisms. However, since the focus of the reconnection community has been primarily on the study of energetic electrons, there have been only a few studies of bulk electron heating during reconnection. In some solar flares, the bulk electron heating may not be important because most of the electrons may become non-thermal. In the magnetotail and in laboratory experiments, on the other hand, electron thermal energy is more important because the population of energetic electrons remains small. Thus, more research focused on understanding electron heating is required and this paper addresses key issues related to non-classical electron heating during collisionless reconnection.

II. EXPERIMENTAL SETUP

Experimental studies described in this paper were carried out on the MRX at the Princeton Plasma Physics Laboratory (PPPL).[35] MRX is a mid-size laboratory device specifically designed for detailed studies of magnetic reconnection. MRX has the unique ability to create discharges with a negligible guide field. In MRX plasmas, the MHD criteria ($S \gg 1$, $L \gg \rho_i$, where S is the Lundquist number; L is the system scale length; and ρ_i is the ion gyro radius) are satisfied in the bulk of plasma, while two-fluid effects exist near the reconnection site. MRX also has versatility in controlling external experimental conditions such as the system size L and the magnitude of the guide field.

Figure 1(a) shows a cutaway view of the MRX vacuum chamber. The local coordinate system used throughout this paper is also shown: R is radially outward, Y is the out-of-plane (symmetric) direction, and Z is the axial direction. The gray circles in Fig. 1(a) indicate the cross sections of the donut-shaped "flux cores" inside of which there are two sets of coils: poloidal field (PF) coils and toroidal field (TF) coils, as shown in Fig. 1(b).[36] The PF coils are wound toroidally to generate the X-line geometry at the middle of the MRX device. Magnetic reconnection is driven by ramping down the PF coil current. This stage of reconnection is called pull reconnection since field lines are pulled toward the flux cores. The TF coils are wound poloidally, such that they produce an inductive electric field to break down the plasma. The distance between the two flux cores can be varied externally. For this study, the surface-to-surface separation between the flux cores is 42 cm, which is about 5 times the ion skin depth, $d_i \approx 8$ cm. No external guide field is applied so that the reconnecting field lines are nearly antiparallel during the quasi-steady period of reconnection over which the reconnection rate remains relatively constant.

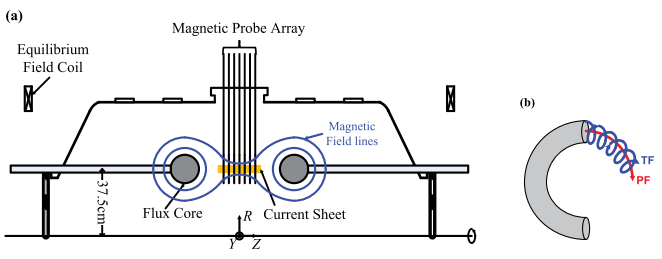

FIG. 1. (a) Toroidal cross section of the MRX vacuum chamber. The gray circles indicate the location of the two flux cores. The orange color denotes the shape of the current sheet formed during pull reconnection. The blue lines are samples of magnetic field lines. (b) Coil windings of the flux core. The PF coils are wound toroidally, while TF coils are wound poloidally.

Extensive sets of diagnostics are employed to study energy conversion processes in MRX. Due to the relatively low electron temperature (≤ 12 eV) and short discharge duration (<1 ms), *in-situ* measurements of plasma quantities are possible in MRX. The evolution of all three components of the magnetic field is measure by a 2-D magnetic probe array that was newly constructed for this experimental campaign. The array consists of 7 probes with a separation of 3 cm along Z. Each probe has 35 miniature pickup coils with a maximum radial resolution of 6 mm. Since the dynamic timescale of the MRX plasma is short ($\sim 1\mu$s), triple Langmuir probes,[37] which do not require a sweep of the bias voltage, are used to measure both the electron temperature (T_e) and density (n_e). The density measurements from the Langmuir probes are calibrated by data from a CO_2 laser interferometer. A radial profile of the floating potential (Φ_f) is obtained from a 17-tip floating potential probe with a maximum resolution of 0.7 cm. A fluctuation probe is utilized to measure fluctuations in all three components of the magnetic field and in the out-of-plane component of the electric field in the lower hybrid frequency range (1–10 MHz). Local ion temperature is measured by ion dynamics spectroscopy probes (IDSPs),[38] which obtain the spectrum of the He II 4686 Å line, which is subsequently fitted to a sum of 13 Gaussian functions in order to take fine structure effects into account;[39] without considering fine structure, the ion temperature is over-estimated by 15%–25%. The signal from the IDSPs passes through a spectrometer with 0.05 Å resolution and is recorded by a gated, intensified charge-coupled device (ICCD) camera. The time resolution of the IDSPs is limited by the gate-open time of 5.6 μs and the spatial resolution is determined by the 3–4 cm distance between the lens and the view dump. These resolutions are required to achieve a sufficient signal-to-noise ratio. Due to their better time and spatial resolution, Mach probes are separately used for measurements of ion flow velocity ($\mathbf{V}_i$). The data from the Mach probes are calibrated by spectroscopic measurements from the IDSPs.

Using extensive R–Z scans of the previously described probes, 2-D profiles of various plasma parameters such as n_e, T_e, T_i, Φ_f, $\mathbf{V}_i$, and electron flow velocity $\mathbf{V}_e$ are obtained. The number of measurement points along the Z direction is 6–7 and the distance between the measurement points is typically 3 cm. Along the radial direction, the electrostatic probes are scanned across 13 measurement points with a 1 cm separation, while the IDSPs are scanned across 7 points

every 2 cm. In order to select the final data set, more than 4200 discharges were scrutinized based on the reproducibility of the data from the 2-D magnetic probe array and a reference Langmuir probe. The main criteria are the location of the X-point, the plasma current, and the density and temperature measured by a reference Langmuir probe. For example, the radial location of the X-point (R_X) traced by the 2-D magnetic probe array is an important criterion to select discharges. For 1 cm radial scans, data from discharges with $37 < R_X < 38$ cm are used. For 2 cm radial scans, discharges with $36.5 < R_X < 38.5$ cm are chosen. As shown in Fig. 2, R_X is reasonably reproducible; about 60% of discharges satisfy the condition $37 < R_X < 38$ cm. This subset is reduced further by the other criteria, leaving about 30% of the 4200 discharges, which are used for creating the 2-D profiles presented in this paper. The data values at each measurement point are determined by averaging over 7–15 discharges. The error bars for each measurement are chosen between the standard deviation of each data set and the uncertainty in measurements, whichever is larger.

Plasma parameters are controlled such that the plasma is in the two-fluid regime, which provides the opportunity to identify energy conversion mechanisms during two-fluid reconnection under a prototypical magnetic geometry in a laboratory plasma. As shown in Fig. 3, the resistivity term ($\eta_{S\perp}J_Y$, where $\eta_{S\perp}$ is perpendicular Spitzer resistivity; J_Y is the out-of-plane component of the current density **J**) accounts for about 10% of the reconnection electric field (E_{rec}) at the X point ($R \approx 37.5$), which means that collisionless effects are the dominant mechanisms that break magnetic field lines at the X point. Outside of the current sheet, the electron Lorentz force term ($\mathbf{V}_e \times \mathbf{B}$, red curve) balances the reconnection electric field, indicating strong two-fluid effects.

To facilitate ion temperature measurements, helium discharges with a fill pressure of 4.5 mT are used. With this fill pressure, effects from electron-neutral collisions are limited since the electron-neutral collision frequency (ν_{en}) is less than the electron-ion collision frequency (ν_{ei}). The total momentum-transfer coefficient for electron collisions with helium neutrals is $\langle\sigma\rangle \approx 6 \times 10^{-8}\,\mathrm{cm}^3/\mathrm{s}$ (Ref. 40) assuming $T_e = 10$ eV. The upper limit of the neutral density with the

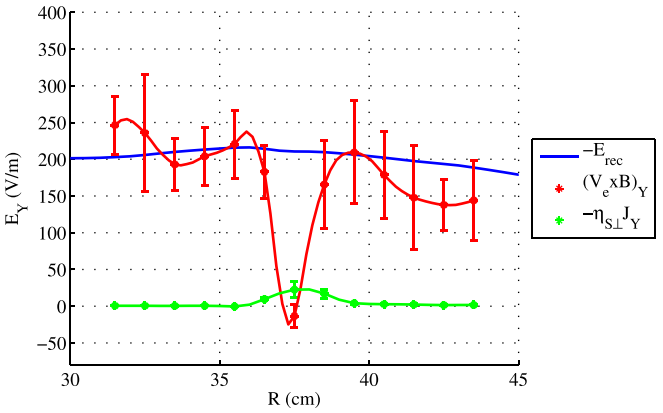

FIG. 3. Radial profile of the out-of-plane electric field at $Z = 0$ in the middle of the quasi-steady period ($t = 332\,\mu$s). The resistivity term is about 10% of the total out-of-plane reconnection electric field at the X point ($R \approx 37.5$ cm), indicating that collisionless effects are dominant in this plasma.

4.5 mT fill pressure is $1.4 \times 10^{14}/\mathrm{cm}^3$, which is the initial neutral density before the plasma is created. The electron-neutral collision frequency ν_{en} is less than 8 MHz. This *upper* bound of ν_{en} is less than the *lower* bound of $\nu_{ei} > 15$ MHz. Furthermore, the neutral density near the X-point is anticipated to be smaller than the initial density due to the high electron temperature and thermal expansion of the neutral gas (neutrals are heated via charge-exchange collisions with ions). Therefore, resistivity due to electron-neutral collisions is estimated to be less than 30% of $\eta_{S\perp}$ and is therefore ignored.

The out-of-plane quadrupole field also supports the existence of strong two-fluid effects in this regime. Figure 4 shows the measured 2-D profile of the quadrupole field. The other side ($Z < 0$) of the quadrupole filed is not shown due to the restricted coverage of the magnetic probes. The maximum magnitude of the quadrupole field reaches 60–70 G, which is about 60%–70% of the reconnecting magnetic field. It is worth noting that the magnitude of the quadrupole field on the outboard side ($R > 37.5$ cm) is about 20% larger than on the inboard side ($R < 37.5$ cm). This is due to a slight asymmetry in the upstream plasma density. The measured 2-D profile of the electron density (not shown) indicates that

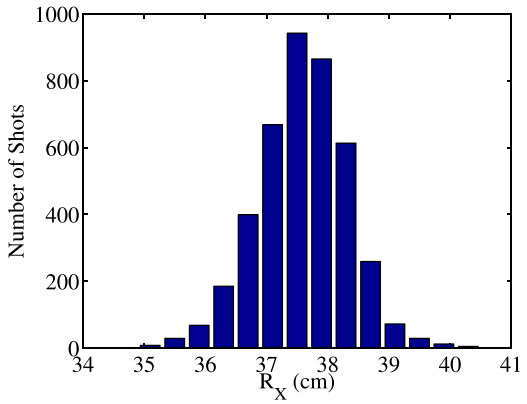

FIG. 2. Histogram of the radial position of the X-point at $t = 330\,\mu$s. The radial location of the X-point (R_X) is an important criterion to select discharges.

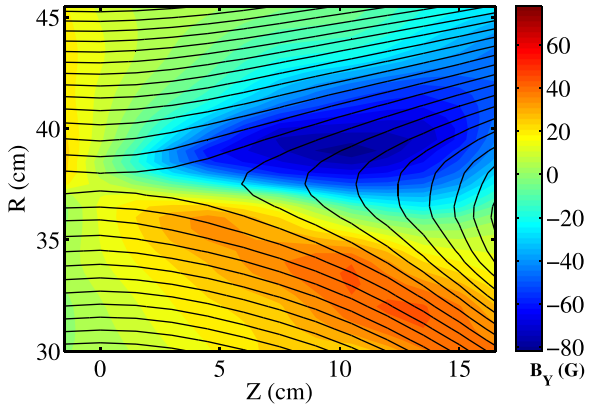

FIG. 4. 2-D profile of the out-of-plane quadrupole magnetic field at $t = 330\,\mu$s along with the contours of the poloidal flux Ψ. Black lines stand for contours of poloidal magnetic flux Ψ.

the outboard density is about 1.7 times larger than the inboard density. The density asymmetry is caused by the in-plane inductive electric field from the time-varying TF currents in the earlier phases of the discharge. The black lines in Fig. 4 are contours of the poloidal magnetic flux $\Psi \equiv \int_0^R 2\pi R' B_Z dR'$, which characterizes the in-plane magnetic field geometry.

III. ION ACCELERATION DUE TO THE IN-PLANE ELECTRIC FIELD

A. In-plane potential profile

As previously introduced, two-fluid effects inside the ion diffusion region lead to the development of the in-plane electrostatic potential that has a well structure along the direction normal to the current sheet. This type of the potential profile is therefore expected to exist in the MRX plasma in the two-fluid regime.

Figure 5(a) shows the measured 2-D profile of the plasma potential Φ_p in the middle of the quasi-steady reconnection period along with contours of the poloidal flux Ψ. The plasma potential is obtained by measuring Φ_f and T_e and using the relation $\Phi_p \sim \Phi_f + (3.3 + 0.5 \ln \mu) T_e$, where

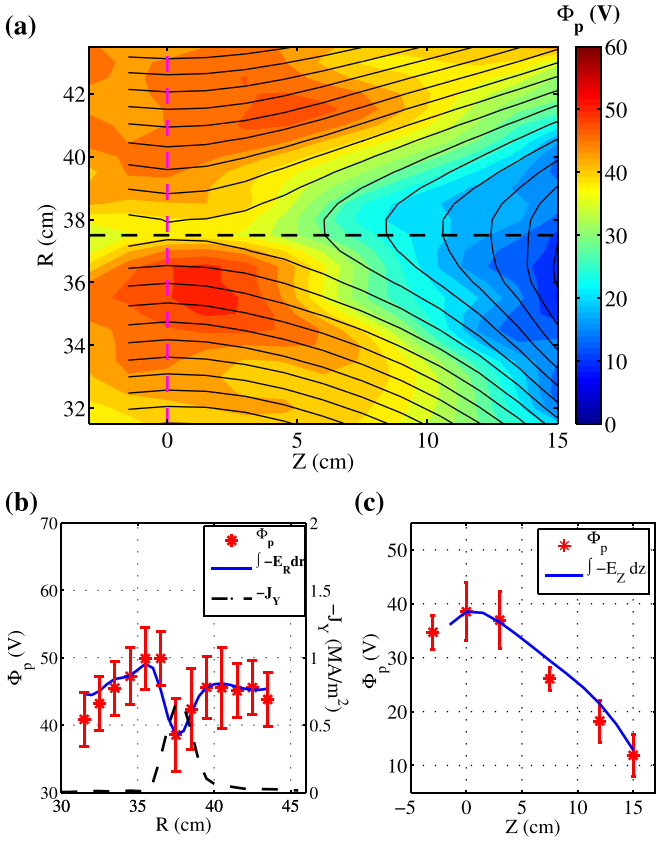

FIG. 5. (a) Measured 2-D plasma potential profile with contours of the poloidal flux Ψ. The radial potential well becomes deeper and wider downstream. (b) Radial profile of Φ_p at $Z = 0$ (along the magenta dashed line in (a)). The red asterisks are the measured Φ_p and the blue line is the radial integration of the right-hand side of Eq. (2). The two profiles are in agreement. The black dashed line indicates the radial J_Y profile at $Z = 0$. (c) Axial profile of Φ_p at $R = 37.5$ cm (along the black dashed line in (a)). The red asterisks are the measured Φ_p and the blue line comes from the integration of the right-hand side of Eq. (4) along Z.

$\mu = m_i/m_p$ and T_e is in units of eV.[41] (The effect from the finite ion temperature is negligible as long as $T_i < 2T_e$,[42] which is mostly satisfied in the MRX discharge.) Fig. 5(b) shows the radial profile of Φ_p at $Z = 0$ (along the magenta dashed line in Fig. 5(a)). At this location, the magnitude of the potential well is about 10 V. The slight asymmetry in the radial potential profile is caused by the aforementioned upstream density asymmetry. The black dashed line shows the radial J_Y profile at the same Z location. It is worth noting that the width of the plasma potential profile is almost the same as that of the current sheet. As shown in Fig. 5(c), the magnitude of the radial potential well becomes deeper downstream, reaching 35 V. It also becomes wider downstream as its boundary expands along the separatrices. These results are consistent with recent numerical simulations.[16–18]

The in-plane potential profile is governed by electron dynamics around the electron diffusion region (EDR). In particular, the in-plane electric field is the result of the electron force balance, and the Lorentz force from electrons accelerated by E_{rec} is the fundamental driving force of the Hall electric field. To test this hypothesis, begin with the electron momentum equation

$$n_e m_e \frac{d\mathbf{V}_e}{dt} = -en_e(\mathbf{E} + \mathbf{V}_e \times \mathbf{B}) - \nabla \cdot \bar{\mathbf{p}}_e + en_e \bar{\eta} \cdot \mathbf{J}, \quad (1)$$

where $\bar{\mathbf{p}}_e$ is the electron pressure tensor and $\bar{\eta}$ is the resistivity tensor. After dropping the negligible electron inertial and resistivity terms, and assuming that the pressure tensor is isotropic, the R component of the above equation at $Z = 0$ leads to

$$E_R \approx -V_{eY} B_Z - \frac{1}{en_e} \frac{\partial p_e}{\partial R}. \quad (2)$$

Since both B_R and B_Y are small at $Z = 0$, the out-of-plane component of the electron diamagnetic drift V^*_{eY} can be approximated as $V^*_{eY} \equiv (\nabla p_e \times \mathbf{B})_Y / (en_e B^2) \approx -(1/en_e B_Z) \partial p_e / \partial R$. Then, Eq. (2) can be rewritten as

$$E_R \approx -(V_{eY} - V^*_{eY}) B_Z. \quad (3)$$

In this MRX plasma, the diamagnetic drift term is not negligible due to strong electron heating near the current sheet that cannot be explained by classical Ohmic heating. This non-classical electron heating will be discussed in Sec. V. The radial electric field reverses sign at the X point where the sign of B_Z also reverses. This indicates that the bipolar radial electric field is the result of electron force balance.[43] Since the total out-of-plane electron flow velocity V_{eY} contains the diamagnetic component, Eq. (3) implies that the electron diamagnetic drift does not contribute to E_R; only pure acceleration by E_{rec} plays a role.[44] By integrating the right-hand side of Eq. (3) along R, the radial potential profile can be estimated. The electron flow velocity is obtained by $\mathbf{V}_e = -\mathbf{J}/en_e + \mathbf{V}_i = -\nabla \times \mathbf{B}/\mu_0 en_e + \mathbf{V}_i$. As shown in Fig. 5(b), the estimated values from Eq. (3) (the blue line) agree with the measured values (red asterisks).

This analysis can be extended in the outflow direction as well. The electron momentum equation along the outflow direction at $R = 37.5$ cm yields

$$E_Z \approx V_{eY} B_R - \frac{1}{en_e}\frac{\partial p_e}{\partial Z}. \quad (4)$$

As electrons flow out of the EDR with high V_{eY}, they create a further potential decrease along the outflow direction Z. The amount of the further potential decrease can be estimated by integrating Eq. (4) along Z, which agrees with the measured values as shown in Fig. 5(c). Due to the high mobility of electrons, the potential drop around the EDR is conveyed along magnetic field lines, creating a strong $\mathbf{E}_{in}$ near the separatrices as shown in Fig. 5(a).

In addition to estimating the structure of the potential well, we can also look at how it may vary with key parameters such as the plasma density n_e and the shoulder value of the reconnecting magnetic field B_{sh}. The radial potential well magnitude $\Delta\Phi_p$ at $Z=0$ can be obtained by integrating Eq. (2) as

$$\Delta\Phi_p = -\int dR\, E_R \approx \int dR \frac{1}{en_e}\left(J_Y B_Z - \frac{\partial p_e}{\partial R}\right)$$
$$\approx \frac{B_{sh}^2}{2\mu_0 e\langle n_e\rangle} + \Delta T_e, \quad (5)$$

where $\langle n_e\rangle$ is the electron density averaged over the current sheet, and ΔT_e is the electron temperature difference between the center of the current sheet and a point just outside. Here, the n_e profile is assumed to have a weak radial dependence; this assumption is substantiated by experimental measurements. This equation indicates that larger potential wells are expected in low density plasmas such as those found in the magnetotail.[13]

The scaling in Eq. (5) is verified experimentally by measuring the depth of the potential well in a series of discharges with different electron densities. In particular, the electron density at the current sheet center is varied by changing the He fill pressure and the PF current waveform is adjusted to maintain the shoulder value of the reconnecting magnetic field at $B_{sh}=100$ G. As shown in Fig. 6, $\Delta\Phi_p - \Delta T_e$ decreases as the electron density in the current sheet increases. The red dashed curve illustrates the expected magnitude from Eq. (5). This scaling can be used to estimate the potential well magnitude when the magnitude of the reconnecting magnetic field and the average density are known.

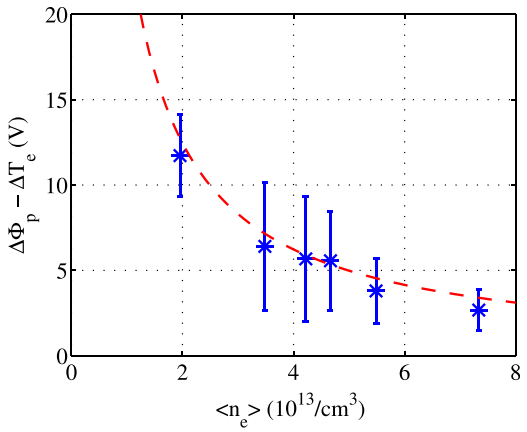

FIG. 6. Dependence of the plasma potential well magnitude on the electron density and temperature at $Z=0$. The red dashed line is the anticipated value of $\Delta\Phi_p - \Delta T_e$ by Eq. (5).

B. Ion acceleration by the in-plane electric field

The in-plane potential profile presented in Subsection III A shows that a strong in-plane field exists throughout the downstream region and is strongest near the separatrices. A typical magnitude of $\mathbf{E}_{in}$ is ~700 V/m, which is much larger than the out-of-plane reconnection field $E_{rec} \sim 200$ V/m.

The strong Hall electric field ballistically accelerates ions near the separatrices since the spatial scale of the Hall electric field (~2 cm) is smaller than the ion gyro-radius (~5 cm). Fig. 7 shows 2-D in-plane flow vectors measured by Mach probes along with contours of Φ_p. Considerable changes in the ion flow occur near the separatrices where ions are accelerated and turn into the outflow direction. It is worth noting that the radial stagnation point of the ion inflow is shifted to the inboard side ($R<37.5$), which is caused by the aforementioned upstream density asymmetry.[45]

The downstream flow energy of ions remains low despite the large potential drop across the separatrices. The maximum ion outflow of 16 km/s corresponds to 5 eV of energy per helium ion, which is much smaller than the magnitude of the potential decrease across the separatrices (≳30 V). The potential drop along the central axis of the outflow region is more than 20 V, which is enough to accelerate ions up to the Alfvén velocity. This indicates that ions must lose considerable momentum as they pass through the downstream region.

One possible cause of the observed sub-Alfvénic ion outflow is the high downstream pressure. The measured downstream ion pressure is 2–4 times larger than the upstream pressure because of both the higher density and the ion heating in the downstream region. Thus, ions must do work on the ambient plasma as they exit the reconnection layer. In this case, the amount of energy lost per ion due to the high downstream pressure ranges from 10–20 eV,

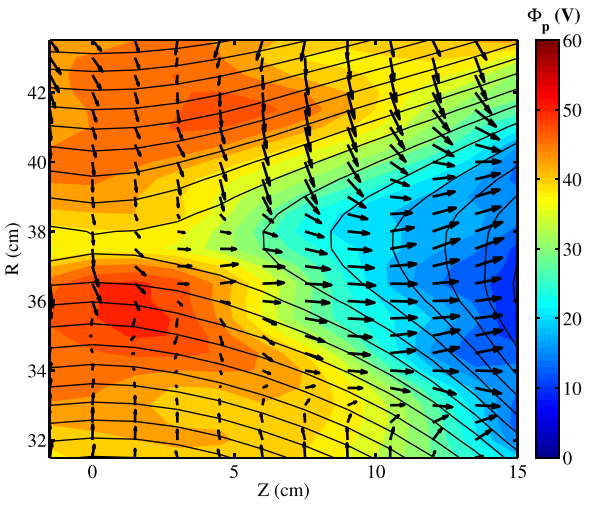

FIG. 7. In-plane ion flow vectors along with contours of Φ_p and Ψ. The flow vectors are measured every 1 cm along R and every 3 cm along Z. The maximum ion velocity is 16 km/s. As ions flow across the separatrices, they are accelerated by $\mathbf{E}_{in}$ and turned into the outflow direction.

depending on the path of the ion. This momentum loss is related to the observed ion downstream heating that will be discussed in Sec. IV.

Another possible cause of the sub-Alfvénic ion outflow is frictional drag by neutrals.[46] With the upper bound of the neutral density of $1.4 \times 10^{14}/\text{cm}^3$, the expected energy loss to neutrals per ion is estimated to be 7–10 V, which is not negligible. However, precise measurements of the neutral density profile are required to verify this neutral effect.

Due to the large in-plane electric field and corresponding ion acceleration, ions obtain energy from the Hall electric field, which agrees with recent simulation results.[18,47] Figure 8 shows the profile of the work done by the electric field on the ions per unit time and unit volume, $\mathbf{J}_i \cdot \mathbf{E}$. The work done by $\mathbf{E}_{in}$ is localized downstream and strongest around the separatrices with values of about $30\,\text{W/cm}^3$. On the other hand, the work done by E_Y is fairly uniform over the measurement region, which is inside the ion diffusion region and has a smaller magnitude of about $5\,\text{W/cm}^3$. The uniform profile of $J_{iY}\,E_Y$ is due to the relatively constant V_{iY} ($\sim$7 km/s) and E_Y ($\sim$200 V/m) profiles.

IV. DOWNSTREAM ION HEATING

Ion temperature is measured by the IDSPs. By varying the direction of the line-of-sight of the IDSP, ion temperatures along the R, Y, and Z directions are separately measured to examine possible ion temperature anisotropy in the MRX plasma. Ion temperatures along each direction will be referred to as T_{iR}, T_{iY}, and T_{iZ}, respectively. The average ion temperature T_i is defined as $(T_{iR} + T_{iY} + T_{iZ})/3$. The ability of the ICCD camera to record two images during a discharge is utilized to monitor the change in temperature profile during the quasi-steady reconnection period. The first image is taken just before the quasi-steady period ($t = 310\,\mu$s), and the second image is obtained in the middle of the period ($t = 330\,\mu$s).

Before the quasi-steady period, the ion temperature is fairly flat and no significant differences among T_{iR}, T_{iY}, and T_{iZ} are observed. As shown in Figs. 9(a) and 9(b), both the Z profile of the ion temperature at $R = 37.5$ cm and the radial profile of T_i at $Z = 15$ cm are relatively uniform.

At the later time of $t = 330\,\mu$s, on the other hand, ion heating is observed downstream. As shown in Fig. 9(c), the ion temperature starts to rise at $Z = 9$ cm. The increase is most prominent in T_{iZ}, which peaks at $Z = 15$ cm. The radial ion temperature profile at $Z = 15$ cm in Fig. 9(d) also shows clear downstream ion heating. All three components of the ion temperature peak at the radial center of the outflow region ($R = 37.5$ cm). Since ion acceleration is weak in the region where ions are heated, these profiles suggest that energy from $\mathbf{E}_{in}$ is primarily used to heat ions further downstream.

The observed downstream heating cannot be explained by classical viscous damping in the *unmagnetized* limit. First, the region where ions are heated does not match the area where classical viscous damping is strong. Based on the theory of Braginskii,[48] the viscous damping is strong where large velocity shear and/or acceleration exist. According to the measured velocity profiles, the viscous damping is actually strongest near the separatrices where ions are significantly accelerated. Furthermore, ion heat conduction is too large to sustain the observed ion temperature profile. The estimated heat conduction at $(R,Z) = (37.5,15)$ is about a factor of 10 larger than the estimated viscous heating power at the same location. These results suggest that the magnetic field may play an important role in the downstream ion heating.

The magnetic field influences the ions via a process called re-magnetization. As the magnetic field becomes stronger further downstream ($Z > 12$ cm), the ions exit the diffusion region and their trajectory is significantly affected by the magnetic field. The ion gyro-motion prolongs the transit of the ions through the outflow region, significantly increasing the chance that ions are thermalized via collisions and/or scattered by wave-particle interactions.

In the downstream region of MRX, ions are efficiently thermalized by re-magnetization and collisions. The plasma becomes more collisional downstream since the downstream plasma density ($5–8 \times 10^{13}/\text{cm}^3$) is higher than the upstream density ($1–2.5 \times 10^{13}/\text{cm}^3$). However, collisions alone are not sufficient to account for the observed heating since ions would exit the downstream region after typically only one or two collisions if their trajectories were not affected by the magnetic field.

Since ion heating by re-magnetization requires analysis of individual ion trajectories, it is difficult to verify this mechanism experimentally. Thus, 2-D fully kinetic simulations were performed to help understand how ions are heated

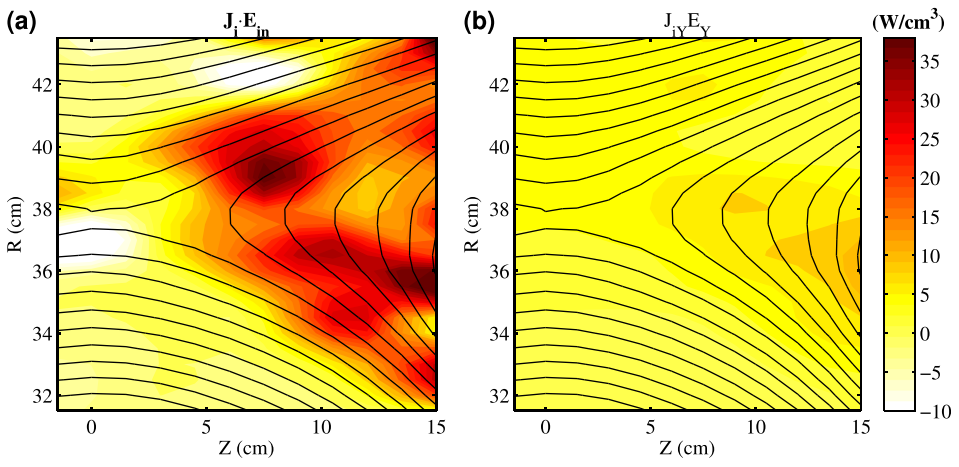

FIG. 8. (a) Work done by the Hall electric field on ions per unit time unit volume ($\mathbf{J}_i \cdot \mathbf{E}_{in}$). It is localized downstream and strongest around the separatrices. (b) Work done by the reconnection electric field ($J_Y\,E_Y$) on ions per unit time and unit volume. It is relatively small and uniform over the measurement region.

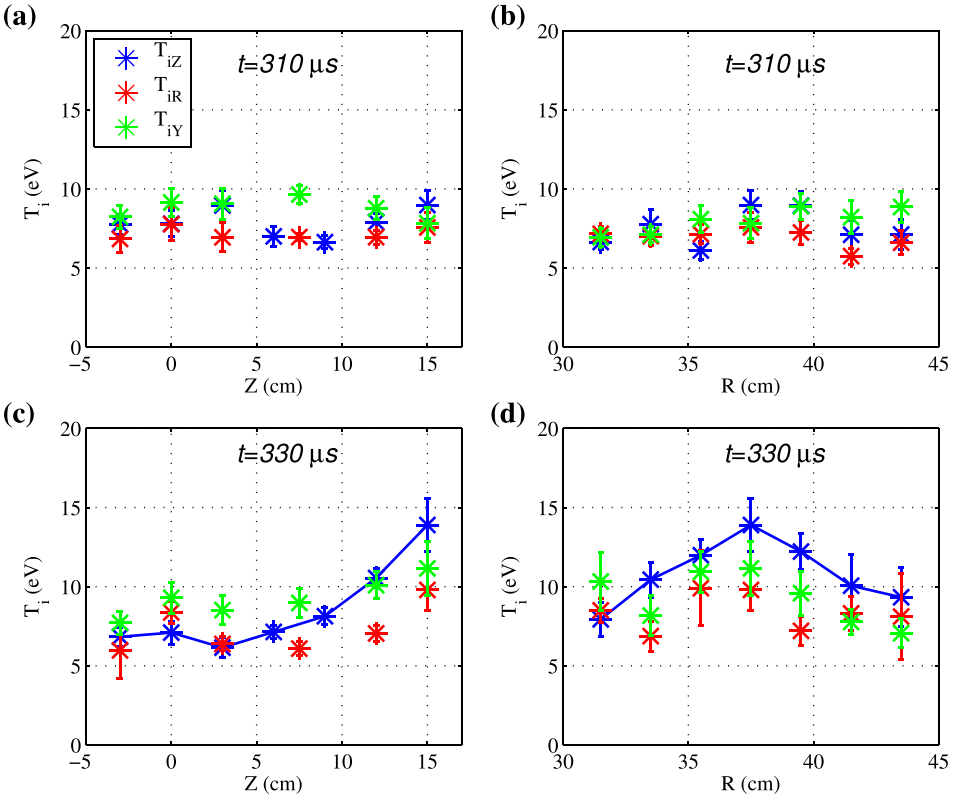

FIG. 9. Measured ion temperature profiles. (a)/(c) Axial profile of each component of T_i at $R = 37.5$ cm at $t = 310$ and 330 μs, respectively. (b)/(d) Radial profile of ion temperature at $Z = 15$ cm at $t = 310$ and 330 μs, respectively. At $t = 310$ μs, the T_i profiles are relatively flat and no significant differences among T_{iR}, T_{iY}, and T_{iZ} exist. At the later time, ions are heated downstream and T_{iZ} becomes hottest there.

downstream. In these simulations, global boundary conditions are similar to the actual MRX geometry. For example, two flux cores and reconnection drive from the decreasing PF coil are implemented in the particle-in-cell (PIC) code VPIC.[49] The coordinate system in the simulations is (x,y,z), corresponding (R,Y,Z) in the MRX coordinate system. A detailed discussion on the boundary conditions can be found in Ref. 50. In addition, Coulomb collisions are modeled using the Takizuka-Abe particle-pairing algorithm.[51] More discussion on the collision operator implementation can be found in Refs. 52 and 53. In the simulations with collisions, we make ion-ion collisions realistic, such that ν_{ii}/Ω_{ci} and $\lambda_{i,mfp}/d_i$ match the experimentally measured values, where ν_{ii} is the ion-ion collision frequency, Ω_{ci} is the upstream ion cyclotron frequency, and $\lambda_{i,mfp}$ is the ion mean free path. The mass ratio in the simulations is $m_i/m_e = 400$, and the initial electron thermal velocity is $0.183\,c$ with $T_i = T_e$. As in the experiment, there is no guide field in the simulations.

Figure 10(a) shows the 2-D profile of the ion temperature in a simulation with realistic ion-ion collisions. The ion temperature is defined as $T_i = (p_{i,xx} + p_{i,yy} + p_{i,zz})/3n_i$, where p_i stands for components of the ion pressure tensor $\bar{\mathbf{p}}_i$. Ion heating is observed broadly over the downstream region, which is consistent with the experimentally measured ion temperature profile. The only significant difference between the experiment and simulation is the ion temperature near the X point. In the simulation, the effective ion temperature along the normal direction $T_{ix} \equiv p_{i,xx}/n_i$ is high due to the counter-streaming ion beam structure caused by the bipolar normal electric field.[13,54] Due to the limited spatial and temporal resolutions of the IDSP measurement, these kinetic effects are not captured in the experimental data.

To quantify the effect from collisions in the observed ion heating, the ion temperature profile in a simulation without collisions is obtained as shown in Figure 10(b). In this simulation, the kinetic effects from the characteristic bounce motion of the ions inside the potential well[29,54] are dominant. The most significant difference between the two profiles is that the simulation without collisions has a higher ion temperature around the X point. The radial potential well magnitude around the X point is about twice as large in the collisionless simulation due to a density depletion near the X-point.[50] With a larger potential well magnitude, T_{ix} is much higher in the collisionless simulation than in the simulation with collisions because the separation between the counter-streaming beams is larger as shown in Fig. 10(d).

Ion velocity space $(v_z\text{-}\ v_x)$ distributions at four different locations are shown in Fig. 10. Shifted Maxwellian distributions are observed upstream at $(z,x) = (0,0.8d_i)$ as shown in Fig. 10(c). It is worth noting that $T_{iz} > T_{ix}$ in the collisionless simulation due to mirror trapping effects. At the X-point (Fig. 10(d)), clear counter-streaming ion beams are observed in both simulations. Near the separatrix (Fig. 10(e)), ions are accelerated along the outflow direction. The ion distribution functions are generally complicated near the separatrices because they are a mixture of ions that undergo a range of different bounce motions.[54] Finally, there are clear differences between the two simulations further downstream $(z,x) = (3d_i,0)$ as shown in Fig. 10(f). With realistic collisions, ions are almost fully thermalized with a higher T_i than the upstream value. In the collisionless simulation, on the other hand, the ion distribution is still highly structured, although clear broadening in the ion distribution exists when compared to the distribution at the X-point. These results indicate that collisions play an important role in downstream

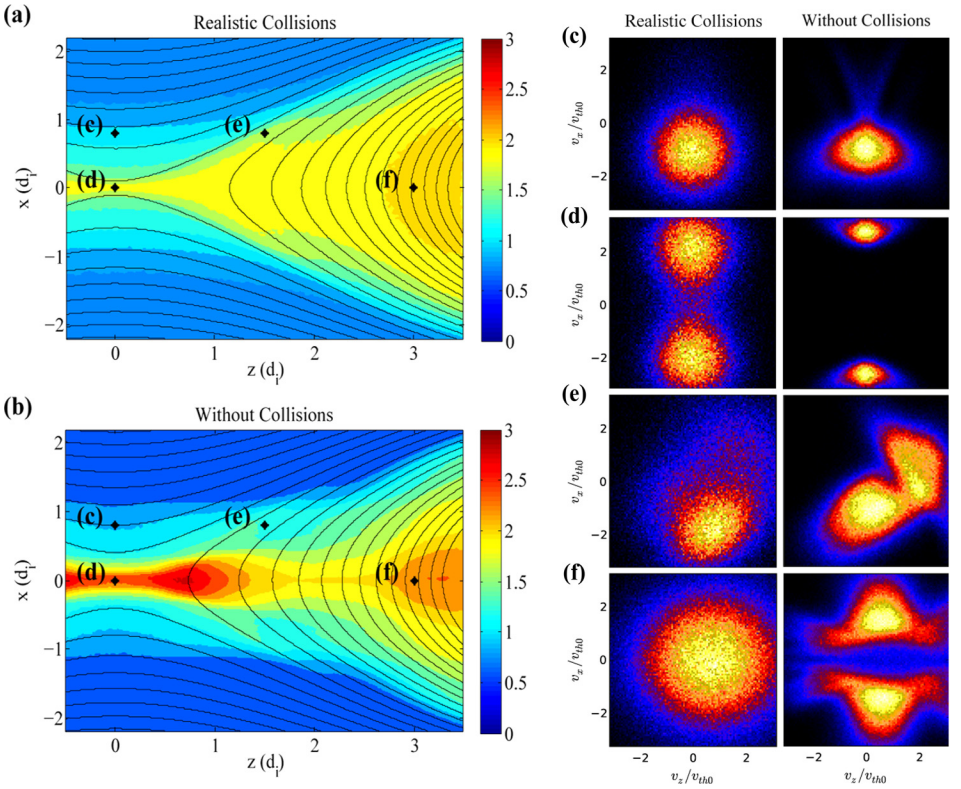

FIG. 10. 2-D ion temperature profiles and ion velocity space distributions. (a) Ion temperature profile from a simulation with realistic ion-ion collisions. The value is normalized to the initial ion temperature. Ions are heated downstream via re-magnetization and collisions. (b) Ion temperature profile from a simulation without collisions. (c), (d), (e), and (f)—Ion velocity space distributions at $(z,x) = (0,0.8d_i)$, $(z,x) = (0,0)$, $(z,x) = (1.5d_i, 0.8d_i)$, and $(z,x) = (3d_i, 0)$, respectively. The ion velocity is normalized to the initial ion thermal velocity, v_{th0}.

ion thermalization in the MRX plasma, but also that ions can still be thermalized to some extent without collisions possibly by the mixing of ions with different trajectories.[54]

V. NON-CLASSICAL ELECTRON HEATING

Electrons are significantly heated during two-fluid reconnection in MRX. Figure 11 shows the 2-D electron temperature profile measured by a triple Langmuir probe. The upstream electron temperature is 5–7 eV. Across the separatrices, electrons are heated up to 11–12 eV. The electron temperature is highest just outside of the electron diffusion region $(Z \approx 6\,\text{cm})$, which suggests that heat is generated near the electron diffusion region. Here, the electron diffusion region is identified by locating the region where the electron frozen-in condition is violated, following Ref. 55. The half width (along R) of the electron diffusion region in this MRX plasma is about 2 cm, and the half length (along Z) is about 6 cm. In addition, a noticeable temperature gradient along the magnetic field implies that significant electron heat flux may exist due to the high parallel thermal conductivity of electrons.

The electron energy gain from the electric field is localized around the X-point. Figure 12 represents the 2-D profile of the work done by the electric field on the electrons per unit time and unit volume, $\mathbf{J}_e \cdot \mathbf{E}$, at $t = 330\,\mu$s. Unlike ions

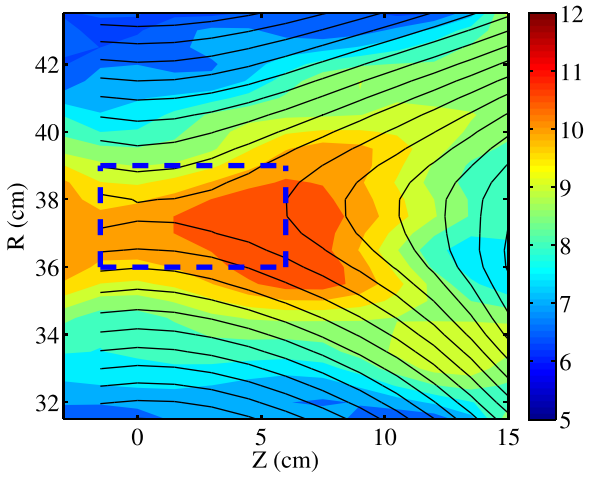

FIG. 11. 2-D electron temperature profile measured by a triple Langmuir probe along with the contours of the poloidal flux Ψ. The upstream electron temperature is 5–7 eV, while the downstream electron temperature reaches up to 11–12 eV. The blue dashed box stands for the region where the energy transport analysis is applied.

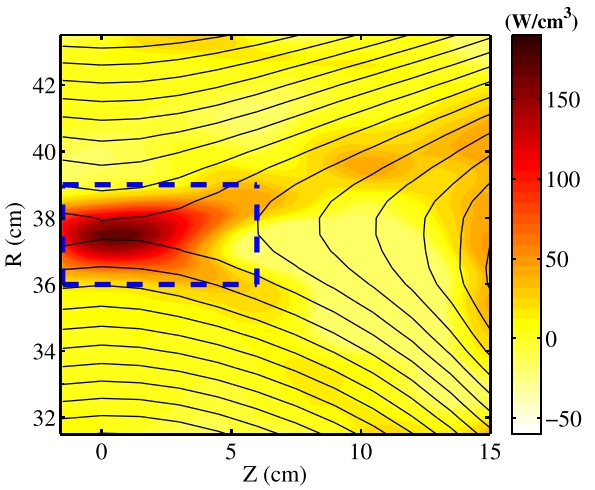

FIG. 12. Work done by the electric field on elections per unit time and unit volume ($\mathbf{J}_e \cdot \mathbf{E}$). Unlike ions, electrons gain energy mostly from the reconnection electric field, and it is localized near the X-point.

that gain energy mostly from the Hall electric field over the broad downstream region, electrons obtain energy mostly from the reconnection electric field in a region that is localized near the X-point. The energy gain inside the small blue dashed box in Fig. 12 accounts for about 70% of the total electron energy gain over the entire measurement region.

Quantitative analyses on electron energy transport near the X-point suggest the existence of anomalous resistivity. To explain both minimal electron flow energy gain and large heat loss due to parallel conduction, there must be efficient heating mechanisms beyond classical Ohmic dissipation.

First, analysis of the electron flow energy transport equation shows that the electron flow energy increase is negligible compared to the total energy gain. The flow energy transport equation for electrons is

$$\frac{\partial}{\partial t}\left(\frac{\rho_e}{2}V_e^2\right)+\nabla\cdot\left(\frac{\rho_e}{2}V_e^2\mathbf{V}_e\right) = \mathbf{J}_e\cdot\mathbf{E}+\mathbf{V}_e\cdot\mathbf{R}_e-\mathbf{V}_e\cdot(\nabla\cdot\bar{\mathbf{p}}_e), \quad (6)$$

where $\rho_e = m_e n_e$, and $\mathbf{R}_e$ is the collisional drag force. By assuming toroidal symmetry, the electron flow energy gain per unit time inside the volume of the plasma ($\mathcal{V}_e$) marked by the blue dashed box in Figs. 11 and 12 can be expressed as

$$W_k = \int_{\mathcal{V}_e}\left[\frac{\partial}{\partial t}\left(\frac{\rho_e}{2}V_e^2\right)+\nabla\cdot\left(\frac{\rho_e}{2}V_e^2\mathbf{V}_e\right)\right]d^3x = (1.8\pm0.4)\times10^3\,(\mathrm{W}). \quad (7)$$

The electron energy gain from the electric field W_{gain} per unit time inside the volume of the plasma ($\mathcal{V}_e$) is calculated as

$$W_{gain} = \int_{\mathcal{V}_e}(\mathbf{J}_e\cdot\mathbf{E})d^3x = \int\int 2\pi R\,dR\,dZ\,(\mathbf{J}_e\cdot\mathbf{E}) = (3.4\pm0.3)\times10^5\,(\mathrm{W}), \quad (8)$$

which is more than two orders of magnitude larger than W_k. Thus, after integrating over $\mathcal{V}_e$, Eq. (6) can be written as

$$\int_{\mathcal{V}_e}\left[\mathbf{J}_e\cdot\mathbf{E}+\mathbf{V}_e\cdot\mathbf{R}_e-\mathbf{V}_e\cdot(\nabla\cdot\bar{\mathbf{p}}_e)\right]d^3x\approx0, \quad (9)$$

since the contribution from the left-hand side is small. This equation suggests two possibilities for the small observed flow energy increase: (1) the collisional drag; and (2) contributions from the divergence of the electron pressure tensor.

In the *classical* limit, the collisional drag term cannot balance the total energy gain. Without considering anomalous resistivity, $\mathbf{R}_e$ can be approximated as $en_e\eta_{S\perp}$, where $\eta_{S\perp}$ is the perpendicular Spitzer resistivity.[56] Then, the work done by the collisional drag force $\mathbf{V}_e\cdot\mathbf{R}_e$ becomes the well-known Ohmic dissipation term $-\mathbf{V}_e\cdot\mathbf{R}_e = -\eta_{S\perp}en_e\mathbf{V}_e\cdot\mathbf{J}\approx\eta_{S\perp}J^2$. The contribution from this term in the volume $\mathcal{V}_e$ is

$$W_{Spitzer} = \int_{\mathcal{V}_e}\eta_{S\perp}J^2d^3x = (5.9\pm1.2)\times10^4\,(\mathrm{W}), \quad (10)$$

which is about 17% of W_{gain}.

The work done by the divergence of the electron pressure tensor $\mathbf{V}_e\cdot(\nabla\cdot\bar{\mathbf{p}}_e)$ is the other candidate for the small electron flow energy increase around the electron diffusion region. It is difficult to evaluate the role of the pressure tensor term directly through experimental measurements since it requires precise measurements of the electron distribution function. Instead, its contribution can be estimated using a model for the nongyrotropic electron pressure tensor.[57] The contribution from the nongyrotropic pressure tensor terms to the reconnection electric field, E_Y^{NG} is

$$E_Y^{NG}\approx\frac{\sqrt{2m_eT_e}}{e}\frac{\partial V_{eZ}}{\partial Z}. \quad (11)$$

With the measured $T_e\sim10\,\mathrm{eV}$ and $\partial V_{eZ}/\partial Z\sim3\times10^6$ /s, E_Y^{NG} is about 32 V/m, which is about the same as the contribution from the resistivity term (~20 V/m) and not enough to balance the reconnection electric field at the X-point (~200 V/m). The total work done by the pressure tensor term over the same volume of plasma is expected to be similar or less than the Ohmic dissipation term, since this term, unlike Ohmic heating, is localized within the small electron diffusion region.

The contribution from the divergence of the electron pressure tensor is estimated to be much smaller in the experiments than in the 2-D simulations. This discrepancy comes from the fact that the measured width of the electron diffusion region is larger than the meandering orbit scale.[50,58] However, there is as of yet no satisfactory physical explanation for this phenomenon. Even after including realistic Coulomb collisions, the width of the layer remains narrower than the measured value.[59] The observed electromagnetic fluctuations propagating at the electron drift velocity near the X-point[32] are also unlikely to resolve this issue, even though similar types of fluctuations are found in 3-D simulations.[53]

Second, analysis of the electron thermal energy transport equation suggests that W_{gain} may be balanced by contributions from the collisional drag term that are larger than the classical Ohmic dissipation. The electron thermal energy transport equation is given by

$$\frac{\partial u_e}{\partial t}+\nabla\cdot(u_e\mathbf{V_e}) = Q_e-p_e\nabla\cdot\mathbf{V_e}-\bar{\pi}_e:\nabla\mathbf{V}_e-\nabla\cdot\mathbf{q}_e, \quad (12)$$

where Q_e is the heat generated by collisions with other species and $\bar{\pi}_e\equiv\bar{\mathbf{p}}_e-p_e\bar{\mathbf{I}}$ is the anisotropic part of the electron pressure tensor. The total internal energy gain per unit time inside $\mathcal{V}_e$ is

$$W_u = \int_{\mathcal{V}_e}\left[\frac{\partial u_e}{\partial t}+\nabla\cdot(u_e\mathbf{V_e})\right]d^3x = (4.9\pm1.0)\times10^4\,(W). \quad (13)$$

The heat generated by collisions with other species Q_e can be approximately equal to the Ohmic dissipation (ηJ^2) since the electron heat loss to ions is negligible due to the long ion-electron collision time ($\gtrsim100\mu$s). Then, the amount of heat obtained by electrons via collisions with other species per unit time, W_{col} becomes

$$W_{col} = \int_{\mathcal{V}_e} Q_e \, d^3x \approx \int_{\mathcal{V}_e} \eta J^2 \, d^3x, \tag{14}$$

where the resistivity η can be either the perpendicular Spitzer value or be anomalous. The second term on the right hand side of Eq. (12) is the compressional heating term. The total amount of compressional electron heating power inside the plasma volume, W_{comp} is

$$W_{comp} = -\int_{\mathcal{V}_e} p_e \nabla \cdot \mathbf{V_e} d^3x = (3.9 \pm 0.8) \times 10^4 \, (W). \tag{15}$$

The next term is the viscous heating term. Since this term is related to $\bar{\pi}_e$, which is difficult to measure directly, we need to estimate the contribution from viscous heating. By noting that $|(\bar{\pi}_e)_{ij}| < p_e$ without the presence of anomalous viscosity and $|(\nabla \mathbf{V}_e)_{ij}| \lesssim |\nabla \cdot \mathbf{V}_e|$, this viscous heating is expected to be on the same order as the compressional heating. As a reference, the Braginskii[48] formulation yields $W_{vis} = (4.3 \pm 0.9) \times 10^4 \, (W)$, which is comparable to W_{comp}.

The final term on the right hand side of Eq. (12) $(\nabla \cdot \mathbf{q}_e)$ represents the energy loss due to microscopic heat flux. The electron heat flux $\mathbf{q}_e$ requires precise information on the electron distribution function. Thus, the heat flux is estimated using results in Ref. 48. Since the electron heat flux is dominated by the parallel heat conduction, $\mathbf{q}_e$ can be approximated as

$$\mathbf{q}_e \approx \chi_{\parallel}^e \hat{\mathbf{b}} (\hat{\mathbf{b}} \cdot \nabla T_e), \tag{16}$$

where $\chi_{\parallel}^e$ is the parallel thermal conductivity, which is a function of n_e and T_e.[48] With this approximation, the total amount of heat loss inside the plasma volume per unit time, W_{loss} is

$$W_{loss} = \int\int 2\pi R \, dR \, dZ \, \nabla \cdot \mathbf{q}_e = (3.0 \pm 1.0) \times 10^5 \, (W), \tag{17}$$

which is larger than other heating terms and comparable to the total energy gain W_{gain} in Eq. (8). The error bars on the electron heat flux are large because, due to the high parallel conductivity, it is sensitive to the electron temperature profile and the electron temperature has error bars of about 1 eV. Although the measurement error is high, W_{loss} is convincingly higher than the integration of any of the other terms in Eq. (12).

Although it is not definitive due to the aforementioned large measurement errors, this massive electron heat flux supports the existence of anomalous resistivity around the X-point. To demonstrate this, apply the volume integral to Eq. (12) to yield

$$W_u = W_{col} + W_{comp} + W_{vis} - W_{loss}. \tag{18}$$

If W_{col} is $W_{Spitzer} = 5.9 \times 10^4$ (W), this equation is not satisfied due to the large energy loss by the heat flux W_{loss}. The value of W_{col} estimated from the above equation is $(2).7 \times 10^5$ (W), which is about 4.5 times larger than $W_{Spitzer}$. This value is large enough to balance the flow energy transport equation (Eq. (6)). Rewriting Eq. (9) yields

$$W_{gain} \approx W_{res} + W_{pe}, \tag{19}$$

where $W_{res} = -\int\int 2\pi R \, dR \, dZ \, (\mathbf{V}_e \cdot \mathbf{R}_e) \approx W_{col}$, and $W_{pe} = \int\int 2\pi R \, dR \, dZ \, \mathbf{V}_e \cdot (\nabla \cdot \bar{\mathbf{p}}_e)$. With $W_{res} = 2.7 \times 10^5$ (W), W_{pe} is about 0.7×10^5 (W), which agrees with the estimate based on Eq. (11). The most important difference between W_{pe} and W_{res} is that W_{pe} cannot contribute to the election thermal energy transport. Thus, to balance both Eqs. (18) and (19), the Ohmic dissipation must be larger than the value based on the Spitzer resistivity, implying the presence of anomalous resistivity.

As a possible candidate for anomalous resistivity, high-frequency magnetic and electrostatic fluctuations are measured by a fluctuation probe. Figure 13(a) shows the 2-D profile of energy in magnetic fluctuations of 1–10 MHz. Although the wave energy is small because the typical fluctuation amplitude is ~5 G, the 2-D profile clearly shows that the fluctuation energy is higher downstream. It does not peak at the X-point but rather at the end of the electron diffusion region where the current density is highest. Similar to magnetic fluctuations, energy in the out-of-plane component of the electrostatic fluctuations increases downstream and does not peak at the X-point. A typical amplitude for the electrostatic fluctuations is ~100 V/m. These profiles indicate that high-frequency fluctuations may contribute to electron thermalization. As electrons move out of the electron diffusion region, they can be effectively thermalized due to these high-frequency fluctuations in the lower hybrid frequency range.

Further research is required to identify non-classical electron heating mechanisms near the electron diffusion

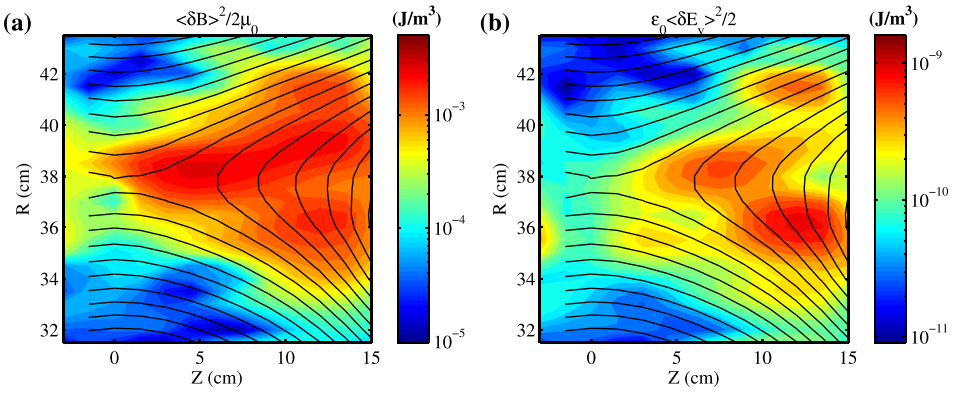

FIG. 13. 2-D profiles of energy in high-frequency (1–10 MHz) fluctuations along with the contours of the poloidal flux Ψ. (a) Energy in high-frequency *magnetic* fluctuations. The fluctuation energy peaks at the edge of the electron diffusion region where the magnitude of the current density is highest. (b) Energy in high-frequency *electrostatic* fluctuations along the out-of-plane direction (δE_Y). Similar to the magnetic fluctuations, fluctuation energy is large downstream.

region. More quantitative analyses are required to confirm possible contributions from the observed fluctuations in the lower hybrid frequency range to the electron heating. Nonlinear interactions between different waves can also heat electrons near the X-point.[60] There could also be other types of fluctuations with higher frequencies, which are not currently measured in MRX but have been observed in space [e.g., Ref. 61] and in the laboratory.[62] High-frequency fluctuations close to the electron plasma frequency f_{pe} may also explain the discrepancy between experiments and simulations since the present simulations with $f_{pe}/f_{ce} \sim \mathcal{O}(1)$ are not suitable to fluctuations in the plasma with $f_{pe}/f_{ce} \gg 1$, which is satisfied in the MRX plasma. Here, f_{ce} is the electron gyro frequency. The dynamics of fine-scale 3-D structures such as flux ropes may also contribute to the non-classical heating through coalescence of the flux ropes.

VI. CONCLUSIONS

Energy conversion from magnetic to particle energy during two-fluid reconnection has been investigated experimentally in MRX. By utilizing various diagnostics including a 2-D magnetic probe array, a multiple-tip floating potential probe, a high-frequency fluctuation probe, Langmuir probes, Mach probes, and ion dynamics spectroscopy probes, 2-D profiles of various physical quantities are obtained. The measured profiles are used to identify energy conversion mechanisms.

For ion heating and acceleration, the in-plane electric field established by the electron dynamics plays an important role as ions gain energy mostly from this field. The measured in-plane electrostatic profile shows a saddle-shaped structure that becomes wider and deeper along the outflow direction. By examining the electron force balance equation, it is shown that the in-plane electric field balances the Lorentz force from the electron flow accelerated by the reconnection electric field near the electron diffusion region. The potential drop around the electron diffusion region is conveyed along the magnetic field lines, creating a strong in-plane electric field near the separatrices and generating the wider potential well downstream. This saddle-shaped in-plane profile agrees with recent numerical simulations [e.g., Refs. 16–18] and space observations [e.g., Refs. 12 and 13]. The radial potential well magnitude is derived from the electron momentum equation, which scales as $B_{rec}^2/\langle n_e \rangle$. This scaling agrees with measurements from discharges with different average density, $\langle n_e \rangle$.

Since the Hall electric field is large (~700 V/m) and has a spatial scale less than the ion gyro-radius, ions are immediately accelerated toward the outflow direction near the separatrices. The maximum outflow speed is about half of the Alfvén velocity $V_A = B/\sqrt{\mu_0 m_i n_c}$, where n_c is the density at the center of the current sheet. Further downstream, ion heating is observed that cannot be explained by classical viscous damping in the unmagnetized limit. The mechanism is identified as the re-magnetization of ions. As ion orbits are affected by the downstream magnetic field, ions stay longer in the diffusion region, which promotes ion thermalization via collisions and possibly scattering by wave-particle interactions. A 2-D PIC simulation with realistic ion-ion collisions shows that collisions can effectively thermalize ions in the MRX plasma. Near the X-point and separatrices, kinetic effects still exist. These kinetic effects are not captured by the current diagnostics (IDSP) due to limited resolution. Different diagnostics with better resolution such as an ion energy analyzer are required to address this problem. In a collisionless simulation, while kinetic effects are dominant in the ion temperature profile, ions are still thermalized downstream to some degree. This ion thermalization in the collisionless limit can be also an interesting future research topic. A possible candidate is scattering by waves.

The 2-D electron temperature profile obtained using triple Langmuir probes shows that electrons are heated around the electron diffusion region. The electron temperature increases sharply across the separatrices and peaks at the edge of the electron diffusion region. This profile suggests that heat is generated around the diffusion region and propagates quickly along the magnetic field lines.

Measurements and analyses suggest that electrons are heated by anomalous resistivity, but the precise mechanisms that generate the anomalous resistivity remain unknown. First, the outgoing electron flow energy from the electron diffusion region remains negligible, although the electron energy gain from the electric field is significant there. Second, classical Ohmic dissipation based on the perpendicular Spitzer resistivity cannot explain the measured 2-D temperature profile. The required heating power exceeds that of classical Ohmic dissipation by a factor of more than four due to the large electron heat flux. To explain the small electron flow energy gain and high electron heat flux at the same time, the dissipation must be larger than the classical value, indicating the presence of anomalous resistivity. Magnetic and electrostatic fluctuations in the lower hybrid frequency range are observed near the X-point and throughout the downstream region. These fluctuations may contribute to the observed non-classical electron heating, but additional measurements on the wave characteristics are required to draw definitive conclusions.

The observed non-classical electron heating is related to an important problem, which is the discrepancy in the width of the electron diffusion layer between experiments and simulations. The experimentally measured width is much larger than that in 2-D simulations.[50,59] Effects from Coulomb collisions contribute to broadening the layer, but its width remains narrow in simulations.[59] Electromagnetic fluctuations traveling along the out-of-plane direction[32] are also found in 3-D simulations but they do not resolve the discrepancy.[53] The possibility of current sheet broadening due to the presence of small, 3-D flux ropes is suggested,[63] but this speculation has not been confirmed. Magnetic fluctuations in the frequency range similar to that in Ref. 32 were observed near the X-point. However, the 2-D profiles of the fluctuation power show that fluctuations are stronger downstream rather than at the X-point. These fluctuations may originate from different types of waves propagating along the magnetic fields, which possibly contribute to the development of anomalous resistivity near the edge of the electron diffusion region. To identify the physical mechanisms behind the

observed non-classical heating and to verify the presence of anomalous resistivity due to the observed fluctuations, more detailed measurements of wave characteristics are necessary. In addition, careful comparisons between experiments and simulations are also required.

ACKNOWLEDGMENTS

This work was supported by DOE Contract No. DE-AC0209CH11466 and NASA program for the MMS mission under the grant No. NNH11AQ45I. The authors thank V. Roytershteyn and W. Daughton for useful discussions regarding the numerical simulations, and R. Cutler for technical support.

[1]E. Priest and T. Forbes, *Magnetic Reconnection—MHD Theory and Applications* (Cambridge University Press, New York, USA, 2000).
[2]E. G. Zweibel and M. Yamada, Annu. Rev. Astron. Astrophys. **47**, 291 (2009).
[3]M. Yamada, R. Kulsrud, and H. Ji, Rev. Mod. Phys. **82**, 603 (2010).
[4]M. Yamada, F. M. Levinton, N. Pomphrey, R. Budny, J. Manickam, and Y. Nagayama, Phys. Plasmas **1**, 3269 (1994).
[5]P. Sweet, *Electromagnetic Phenomena in Cosmical Physics* (Cambridge University Press, New York, 1958).
[6]E. N. Parker, J. Geophys. Res. **62**, 509, doi:10.1029/JZ062i004p00509 (1957).
[7]G. Paschmann, B. U. Ö. Sonnerup, I. Papamastorakis, N. Sckopke, G. Haerendel, S. J. Bame, J. R. Asbridge, J. T. Gosling, C. T. Russell, and R. C. Elphic, Nature **282**, 243 (1979).
[8]J. T. Gosling, M. F. Thomsen, S. J. Bame, and C. T. Russell, J. Geophys. Res. **91**, 3029, doi:10.1029/JA091iA03p03029 (1986).
[9]T. D. Phan, L. M. Kistler, B. Klecker, G. Haerendel, G. Paschmann, B. U. Ö. Sonnerup, W. Baumjohann, M. B. Bavassano-Cattaneo, C. W. Carlson, A. M. DiLellis *et al.*, Nature **404**, 848 (2000).
[10]M. Øieroset, T.-D. Phan, M. Fujimoto, R. P. Lin, and R. P. Lepping, Nature **412**, 414 (2001).
[11]M. A. Shay, J. F. Drake, B. N. Rogers, and R. E. Denton, Geophys. Res. Lett. **26**, 2163, doi:10.1029/1999GL900481 (1999).
[12]F. S. Mozer, S. D. Bale, and T.-D. Phan, Phys. Rev. Rett. **89**, 015002 (2002).
[13]J. R. Wygant, C. A. Carttell, R. Lysak, Y. Song, J. Dombeck, J. McFadden, F. S. Mozer, C. W. Carlson, G. Parks, E. A. Lucek *et al.*, J. Geophys. Res. **110**, A09206, doi:10.1029/2004JA010708 (2005).
[14]M. A. Shay, J. F. Drake, R. E. Denton, and D. Biskamp, J. Geophys. Res. **103**, 9165, doi:10.1029/97JA03528 (1998).
[15]P. L. Pritchett, J. Geophys. Res. **106**, 25961, doi:10.1029/2001JA000016 (2001).
[16]H. Karimabadi, W. Daughton, and J. Scudder, Geophys. Res. Lett. **34**, L13104, doi:10.1029/2007GL030306 (2007).
[17]J. F. Drake, M. A. Shay, and M. Swisdak, Phys. Plasmas **15**, 042306 (2008).
[18]P. L. Pritchett, J. Geophys. Res. **115**, A10208, doi:10.1029/2010JA015371 (2010).
[19]W. Gekelman, R. L. Stenzel, and N. Wild, J. Geophys. Res. **87**, 101, doi:10.1029/JA087iA01p00101 (1982).
[20]M. Brown, C. Cothran, D. Cohen, J. Horwitz, and V. Chaplin, J. Fusion Energy **27**, 16 (2008).
[21]Y. Ono, H. Tanabe, Y. Hayashi, T. Ii, Y. Narushima, T. Yamada, M. Inomoto, and C. Z. Cheng, Phys. Rev. Lett. **107**, 185001 (2011).
[22]Y. Ono, M. Yamada, T. Akao, T. Tajima, and R. Matsumoto, Phys. Rev. Lett. **76**, 3328 (1996).
[23]A. Stark, W. Fox, J. Egedal, O. Grulke, and T. Klinger, Phys. Rev. Lett. **95**, 235005 (2005).
[24]S. C. Hsu, G. Fiksel, T. A. Carter, H. Ji, R. M. Kulsrud, and M. Yamada, Phys. Rev. Lett. **84**, 3859 (2000).
[25]S. Gangadhara, D. Craig, D. A. Ennis, D. J. D. Hartog, G. Fiksel, and S. C. Prager, Phys. Rev. Lett. **98**, 075001 (2007).
[26]G. Fiksel, A. F. Almagri, B. E. Chapman, V. V. Mirnov, Y. Ren, J. S. Sarff, and P. W. Terry, Phys. Rev. Lett. **103**, 145002 (2009).
[27]R. M. Magee, D. J. Den Hartog, S. T. A. Kumar, A. F. Almagri, B. E. Chapman, G. Fiksel, V. V. Mirnov, E. D. Mezonlin, and J. B. Titus, Phys. Rev. Lett. **107**, 065005 (2011).
[28]M. Hoshino, T. Mukai, T. Yamamoto, and S. Kokubun, J. Geophys. Res. **103**, 4509, doi:10.1029/97JA01785 (1998).
[29]J. F. Drake, M. Swisdak, T. D. Phan, P. A. Cassak, M. A. Shay, S. T. Lepri, R. P. Lin, E. Quataert, and T. H. Zurbuchen, J. Geophys. Res. **114**, A05111, doi:10.1029/2008JA013701 (2009).
[30]E. Mobius, D. Hovestadt, B. Klecker, M. Scholer, G. Gloeckler, and F. M. Ipavich, Nature **318**, 426 (1985).
[31]R. L. Stenzel, W. Gekelman, and N. Wild, J. Geophys. Res. **87**, 111, doi:10.1029/JA087iA01p00111 (1982).
[32]H. Ji, S. Terry, M. Yamada, R. Kulsrud, A. Kuritsyn, and Y. Ren, Phys. Rev. Lett. **92**, 115001 (2004).
[33]S. Imada, M. Hoshino, and T. Mukai, Geophys. Res. Lett. **32**, L09101 (2005).
[34]J. Egedal, W. Fox, N. Katz, M. Porkolab, M. Øieroset, R. P. Lin, W. Daughton, and J. F. Drake, J. Geophys. Res. **113**, A12207, doi:10.1029/2008JA013520 (2008).
[35]M. Yamada, H. Ji, S. Hsu, T. Carter, R. Kulsrud, N. Bretz, F. Jobes, Y. Ono, and F. Perkins, Phys. Plasmas **4**, 1936 (1997).
[36]M. Yamada, H. P. Furth, W. Hsu, A. Janos, S. Jardin, M. Okabayashi, J. Sinnis, T. H. Stix, and K. Yamazaki, Phys. Rev. Lett. **46**, 188 (1981).
[37]S.-L. Chen and T. Sekiguchi, J. Appl. Phys. **36**, 2363 (1965).
[38]G. Fiksel, D. J. D. Hartog, and P. W. Fontana, Rev. Sci. Instrum. **69**, 2024 (1998).
[39]W. L. Wiese and J. R. Fuhr, J. Phys. Chem. Ref. Data **38**, 565 (2009).
[40]Y. Itikawa, At. Data Nucl. Data Tables **21**, 69 (1978).
[41]I. H. Hutchinson, *Principles of Plasma Diagnostics*, 2nd ed. (Cambridge University Press, Cambridge, UK, 2005).
[42]I. H. Hutchinson, Plasma Phys. Controlled Fusion **44**, 1953 (2002).
[43]B. Li and R. Horiuchi, Phys. Rev. Lett. **101**, 215001 (2008).
[44]D. A. Uzdensky and R. M. Kulsrud, Phys. Plasmas **13**, 062305 (2006).
[45]P. A. Cassak and M. A. Shay, Phys. Plasmas **14**, 102114 (2007).
[46]E. E. Lawrence, H. Ji, M. Yamada, and J. Yoo, Phys. Rev. Lett. **110**, 015001 (2013).
[47]M. V. Goldman, D. L. Newman, J. T. Gosling, L. Andersson, S. Eriksson, G. Lapenta, and S. Markidis, *paper presented at the 54th Annual APS-DPP Meeting, Providence,* RI, 2012.
[48]S. I. Braginskii, in *Reviews of Plasma Physics* (Consultants Bureau, New York, 1965), Vol. 1, pp. 205–311.
[49]K. J. Bowers, B. J. Albright, L. Yin, B. Bergen, and T. J. T. Kwan, Phys. Plasmas **15**, 055703 (2008).
[50]S. Dorfman, W. Daughton, V. Roytershteyn, H. Ji, Y. Ren, and M. Yamada, Phys. Plasmas **15**, 102107 (2008).
[51]T. Takizuka and H. Abe, J. Comput. Phys. **25**, 205 (1977).
[52]W. Daughton, V. Roytershteyn, B. J. Albright, H. Karimabadi, L. Yin, and K. J. Bowers, Phys. Plasmas **16**, 072117 (2009).
[53]V. Roytershteyn, S. Dorfman, W. Daughton, H. Ji, M. Yamada, and H. Karimabadi, Phys. Plasmas **20**, 061212 (2013).
[54]N. Aunai, G. Belmont, and R. Smets, J. Geophys. Res. **116**, A09232, doi:10.1029/2011JA016688 (2011).
[55]Y. Ren, M. Yamada, H. Ji, S. Dorfman, S. P. Gerhardt, and R. Kulsrud, Phys. Plasmas **15**, 082113 (2008).
[56]A. Kuritsyn, M. Yamada, S. Gerhardt, H. Ji, R. Kulsrud, and Y. Ren, Phys. Plasmas **13**, 055703 (2006).
[57]M. Hesse, K. Schindler, J. Birn, and M. Kuznetsova, Phys. Plasmas **6**, 1781 (1999).
[58]H. Ji, Y. Ren, M. Yamada, S. Dorfman, W. Daughton, and S. P. Gerhardt, Geophys. Res. Lett. **35**, L13106, doi:10.1029/2008GL034538 (2008).
[59]V. Roytershteyn, W. Daughton, S. Dorfman, Y. Ren, H. Ji, M. Yamada, H. Karimabadi, L. Yin, B. J. Albright, and K. J. Bowers, Phys. Plasmas **17**, 055706 (2010).
[60]Y. Wang, Ph.D. thesis, Princeton University, 2010.
[61]A. Vaivads, Y. Khotyaintsev, M. André, and R. Treumann, "Plasma waves near reconnection sites," in *Lecture Notes Physics*, Vol. 687 (Springer, Berlin, Heidelberg, 2006), pp. 251–269.
[62]W. Fox, M. Porkolab, J. Egedal, N. Katz, and A. Le, Phys. Plasmas **17**, 072303 (2010).
[63]S. Dorfman, H. Ji, M. Yamada, J. Yoo, E. Lawrence, C. Myers, and T. D. Tharp, Geophys. Res. Lett. **40**, 233, doi:10.1029/2012GL054574 (2013).